Geometry Numerical Simulation and Analysis for Moon-Based Earth Observation

Guozhuang Shen, *Member, IEEE*, Huadong Guo, *Member, IEEE*, Guang Liu, *Member, IEEE*, Lu Zhang, *Member, IEEE*, and Jing Huang

***Abstract*—Because of their scientific and social significance, large-scale geoscientific phenomena are attracting more and more attention. However, many existing Earth observation systems lack the ability to conduct long-term continuous observations on regional to global scales because of limitations on spatial and temporal coverage and the existence of systematic bias. The geometrical relationship between the Sun, Earth, and Moon is a precondition to understanding the Moon-based Earth observation (MEO). In this study, a geometry numerical simulation system for the MEO is developed based on Jet Propulsion Laboratory ephemerides data, time system transformations, and reference system transformations. Using this system, we study changes of Moon-based sensors (MBSs) subpoints in the year 2016 and from 1901 to 2016, the local azimuth–elevation angle of a point of interest on the Earth at different times in 2016 and throughout that year, and changes in observation duration at four different locations in 2016 and from 1901 to 2016. A nonlinear fitting method is used to analyze the periodic behavior of observation durations. Some factors influencing the MEO geometry are also analyzed, including the influence of the DE data source on MBS's position and on the azimuth–elevation angle of a point of interest on the Earth, the influence of the minimum observation elevation angle on the MBS observation extent, and the influence of the MBS location on the subpoint, azimuth–elevation angle, and observation period. The results show that Moon-based Earth observatory has specific and unique advantages in terms of observation geometry, which makes it suitable for observation of large-scale geoscientific phenomena.**

***Index Terms*—Earth observation, geometry, Moon-based, numerical simulation.**

I. Introduction

LARGE-scale geoscientific phenomena are increasingly attracting attention because of their scientific and social significance [1], [2]. However, many existing Earth observation systems lack the ability to conduct long-term continuous observations on regional to global scales because of limitations of spatial and temporal coverage and the existence of systematic bias. Recently, the Moon, Earth's sole natural satellite, has been proposed as a new platform for Earth observation of large-scale geoscientific phenomena [1]–[5]. The advantages of Moon-based Earth observation (MEO) can be summarized as long-term consistency, integrity, stability, and uniqueness [1], [4].

A variety of Moon-based sensors (MBSs) have been designed and analyzed in recent years. A lunar-based ultraviolet telescope (LUT) has been proposed by Cao *et al.* to continuously monitor variable stars, rather than the Earth [6]. The extreme ultraviolet (EUV) radiation properties of the Earth's plasmasphere have been studied, thereby, providing an important basis for the design of Moon-based EUV imagers [7]. Li *et al.* analyzed the optomechanical design of a lunar-based EUV camera for imaging the Earth [8], and also designed and analyzed a lunar-based tracking turntable for Earth observation [9]. Li *et al.* also presented a thermal design and thermal analysis of a Moon-landed telescope (MLT) [10]. To explore the Earth's plasmasphere from the Moon, Li *et al.* proposed a Moon-landed explorer (MLE) [11]. Nie *et al.* discussed simulation of land surface temperature from the MEO [12]. To monitor radiation from the Earth, Duan *et al.* proposed a conceptual design for Moon-based Earth radiation observation (MERO) [13] and constructed an entrance pupil irradiance (EPI) estimating model for a simplified single-pixel MERO instrument [14].

Synthetic aperture radar (SAR) is an important technique for Earth observation. The features of a possible Moon-based SAR system in terms of imaging characteristics (resolution and power constraints) and potential applications have been investigated, as have its expected limitations [15]. Owing to the unique imaging geometry of Moon-based SAR, Ding *et al.* analyzed a Doppler parameter estimation method that differs from the methods used in conventional pickaback and satellite-borne SAR [16]. A Moon-based interferometric SAR called LUNA ROSSA was presented by Moccia *et al.* The overall system parameters and expected performance of the microwave observatory were computed. Moccia *et al.* also compared the proposed Moon-based observatory to spaceborne interferometric systems, revealing its unique performance characteristics [17]. Xu *et al.* pointed out that for Moon-based SAR, owing to the extremely long exposure time resulting from the complex geometry, conventional SAR imaging techniques are no longer suitable [18]. Although the operating range is much longer than that of spaceborne SAR,

Manuscript received August 9, 2019; revised March 17, 2020 and May 16, 2020; accepted May 17, 2020. Date of publication May 28, 2020; date of current version June 29, 2020. This work was supported in part by the National Natural Science Foundation of China under Grant 41590852, and in part by the Key Research Program of Frontier Sciences, CAS under Grant QYZDY-SSW-DQC026. *(Corresponding author: Guang Liu.)*

The authors are with the Key Laboratory of Digital Earth Science, Aerospace Information Research Institute, Chinese Academy of Sciences, Beijing 100094, China, and also with the University of Chinese Academy of Sciences, Beijing 100864, China (e-mail: shengz@radi.ac.cn; hdguo@radi.ac.cn; liuguang@radi.ac.cn; zhanglu@radi.ac.cn; huangjing181@mails.ucas.ac.cn).

Digital Object Identifier 10.1109/JSTARS.2020.2996613

Moon-based SAR can still obtain higher resolution. The simulated azimuth resolution for L-, C-, and X-band SAR proposed by Fornaro *et al.* can reach to 1.5, 0.7, and 0.5 m separately [15]. The concept of global change observation lunar-based SAR (GCOLB-SAR) was proposed by Guo *et al.* For the GCOLB-SAR, when it operates at C-band (24 cm of wavelength), the simulated azimuth resolution can reach to 1.6–6.9 m, with the 1.6–8.6 m for the range direction [1].

Whatever sensors are arranged on the Moon, the Sun–target (Earth)–sensor (MBS) geometry is a precondition for understanding the MEO. The Satellite Tool Kit (STK, Analytical Graphics, Inc., USA) is the most popular software that can be used to analyze the geometry of the MEO. Zhang *et al.* developed a Sun–Earth–Moon simulation system based on NASA Jet Propulsion Laboratory (JPL) ephemerides DE405 data and OpenGL, which has been used to statistically analyze observation geometry [19]. Home Planet can also be used to do some simple analysis of the geometry [20]. Ren *et al.* developed a simulation system for the MEO based on a simplified geometrical model and proposed an effective coverage parameter for assessing the optical coverage ability of the MEO [5]. Ye *et al.* proposed a geometric model for a Moon-based platform based on Earth orientation parameters and JPL Development Ephemeris (DE) data using a formula describing the relative position of the platform and the Earth observation target. Three key parameters, namely, the visibility of the Earth from the Moon, the nadir point, and the Earth viewing angle, are calculated using the proposed model [21]. Ding *et al.* calculated the coverage indicators and compared these indicators for sensors on a geostationary satellite, on the Moon, and at the Earth–Sun L1 point. Ding *et al.* concluded that the Moon offers much better angular coverage, which is of great significance with regard to the ability of multiangle remote sensing and the observation system to detect the Earth's energy balance [22]. Ye *et al.* proposed a Moon-based observation platform and briefly discussed the performance of the system parameters and with a focus on the potential applications to monitoring the three polar regions (the Arctic, Antarctic, and Tibet Plateau) [23].

In this study, a geometry numerical simulation system is implemented under Microsoft. NET framework using the C# language, combining JPL ephemerides data, a time system transformation, and a reference system transformation. Some observational geometry parameters are also analyzed using this system. Finally, the influences of the DE data source, minimum observation elevation angle, and MBS location on the MEO geometry are analyzed.

II. Data and Methods

As the Sun, Earth, and Moon move in their orbits, their relative positions change over time. To simulate and analyze the observational geometry of the MEO, we must know how to get the precise position and velocity of the Sun, Earth, and Moon, how to perform the transformation between the different time reference systems, and how to perform the transformation between the different spatial reference systems. Here, we construct a simulation system under the Microsoft. NET framework using C# language.

A. Ephemerides Data

As mentioned previously, positions and velocities are needed to simulate the observational geometry of the MEO. An ephemeris can give the positions of naturally occurring astronomical objects as well as artificial satellites in the sky at a given time or times [24].

Reflecting the continuing influx of new data and observations, the JPL has revised its published ephemerides nearly every year for the past 20 years [25]. Therefore, the JPL DE series are the most popular ephemerides among the international astronomical community. The JPL ephemerides provide planetary 3-D Cartesian reference data based on the heliocentric reference system in the form of Chebyshev interpolation polynomials, which contain Chebyshev interpolation polynomial coefficients of a certain time span [26]. DE405 was released in 1998 [27]. It added several years' extra data from telescopic, radar, spacecraft, and very long baseline interferometry (VLBI) observations (of the Galileo spacecraft at Jupiter, in particular). The method of modeling the asteroids' perturbations was improved, although the same numbers of asteroids were modeled as previously. The ephemeris was more accurately oriented onto the International Celestial Reference Frame (ICRF). DE405 covered the years 1600–2200 to full precision. DE421 was released in 2008 [26]. It included additional ranging and VLBI measurements of Mars spacecraft, new ranging and VLBI of the Venus Express spacecraft, the latest estimates of planetary masses, additional lunar laser ranging, and two more months of CCD measurements of Pluto. DE421 covered the years 1900–2050. STK numerical analysis data (calculated from the internal analytic model) were provided in the STK software, and can also be used to position central bodies.

Here, the STK numerical analysis data and JPL DE405 and DE421 data were selected as the data sources to provide positions and velocities. Moreover, they will be compared to show the differences among them when used to simulate the observation geometry for the MEO.

B. Time System Transformation

Because the position and velocity of Sun, Earth, and Moon are time varying, and the JPL DE data were constructed based on the Julian time system, all the time variables are converted to Julian time.

Letting GD be the Gregorian time, JD the Julian time, Y the year part of GD, M the month part of GD, D the day part of GD, H the hour part of GD, Min the minute part of GD, and S the second part of GD, we obtain JD as follows:

$$\begin{aligned} E &= \mathrm{INT}[365.23 \times Y] \\ F &= \mathrm{INT}[30.6001 \times (M+1)] \\ h &= (H + \mathrm{Min}/60 + S/3600)/24 \\ \mathrm{JD} &= E + F + D + h + 1720981.5 \end{aligned} \tag{1}$$

where $\mathrm{INT}[x]$ is the function that gives the integer part of a number x ($\mathrm{INT}[x] \leq x$). If $M > 2$, then Y and M will remain unchanged, but when $M = 1, 2$, we will have $Y = Y - 1$ and $M = M + 12$.

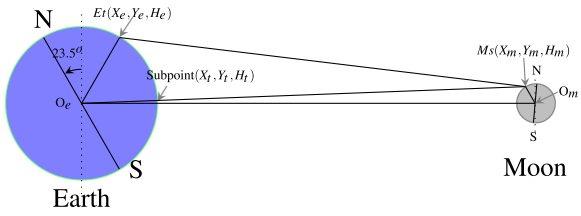

Fig. 1. Geometric diagram for the MEO. O_e is the geocenter, O_m is the selenocenter, the sensor is located at $Ms(X_m, Y_m, H_m)$, the observed target is at $Et(X_e, Y_e, H_e)$, and the subpoint is at (X_t, Y_t, H_t). Note that the Earth–Moon distance is not to scale.

To convert Julian time back to Gregorian time, we perform the following steps:

$$\begin{aligned} a &= \mathrm{INT}[\mathrm{JD} + 0.5] \\ b &= a + 1537 \\ c &= \mathrm{INT}[(b - 122.1)/365.25] \\ d &= \mathrm{INT}[365.25 \times c] \\ e &= \mathrm{INT}[(b - d)/30.6001] \\ f &= b - d - \mathrm{INT}[30.6001 \times e] + \mathrm{FRAC}[\mathrm{JD} + 0.5]. \end{aligned} \tag{2}$$

We then obtain

$$\begin{aligned} D &= \mathrm{INT}[f] \\ H &= \mathrm{INT}[(f - D) * 24] \\ \mathrm{Min} &= \mathrm{INT}\{[(f - D) * 24 - H] * 60\} \\ S &= [(f - D) * 24 - H] * 3600 - \mathrm{Min} * 60 \\ M &= e - 1 - 12 \times \mathrm{INT}[e/14] \\ Y &= c - 4715 - \mathrm{INT}[(7 + M)/10] \\ N &= \mathrm{MOD}\{\mathrm{INT}[\mathrm{JD} + 0.5], 7\}. \end{aligned} \tag{3}$$

Here, $\mathrm{FRAC}[x]$ is the function that gives the fractional part of x, and $\mathrm{MOD}[x, y]$ is the function that gives the remainder when x is divided by y. N is the number of the day of the week: 0 for Monday, . . ., 6 for Sunday.

C. Reference System Transformation

There are a number of reference systems related to the MEO. It is essential to handle the different reference systems for calculating the positions of celestial bodies from different perspectives. To perform the simulation and analysis, the heliocentric celestial reference system (HCRS), geocentric celestial reference system (GCRS), selenocentric celestial reference system (SCRS), principal axis lunar reference system (PALRS), and international terrestrial reference system (ITRS) are adopted. Ren *et al.* described transformations between the reference systems in detail, including those from HCRS to GCRS, GCRS to SCRS, SCRS to PALRS, ITRS to GCRS, and the body reference system to PALRS [5].

Fig. 1 is the geometric diagram for the MEO. We can see that to transform the point position $Ms(X_m, Y_m, H_m)$ in the PALRS to the position in the ITRS at a particular epoch, the following steps must be performed:

1) transform the point position Ms from the lunar fixed system to the SCRS, Ms';
2) transform Ms' from the SCRS to the GCRS, Ms'';
3) perform a rotation from the GCRS to the ITRS, Ms'''.

After these transformation, all the coordinates are expressed in the same reference frame, so we can analyze the geometrical relationship between the MBS and the region of interest on Earth.

For the MBS, a sensor coordinate system must be defined. Then, the position of the platform must also be given in terms of (longitude and latitude). To analyze the observation geometry in the Earth coordinate system, six kinds of basic coordinate systems [sensor coordinate system, selenographic coordinate system, Moon-centered Moon-fixed coordinate system (MCMF), inertial selenocentric coordinate system (MCI), Earth-centered inertial coordinate system (ECI), and Earth-centered Earth-fixed coordinate system (ECEF)] are used; the transformations can also be found in [28]. We have

$$\begin{aligned} P_{\mathrm{ECEF}} &= \mathbf{M}_{\mathrm{ECEF}}^{\mathrm{ECI}}(\Pi, \Theta, \mathrm{N}, \mathbf{P})\mathbf{T}_{\mathrm{ECI}}^{\mathrm{MCI}}(t) \\ &\mathbf{M}_{\mathrm{MCI}}^{\mathrm{MCMF}}(\phi_m, \theta_m, \psi_m)\mathbf{M}_{\mathrm{MCMF}}P_{\mathrm{LOC}}(\phi_L, \xi_L) \end{aligned} \tag{4}$$

where P_{ECEF} and P_{LOC} are the positions of the Moon-based platform position in the ECEF coordinate system and the selenographic coordinate system, respectively, and (ϕ_L, ξ_L) are the location latitude and longitude on the Moon. The transformation from the selenographic coordinate system to the MCMF coordinate system ($\mathbf{M}_{\mathrm{MCMF}}$) requires the location coordinates of the Moon. The Moon orientation information $(\phi_m, \theta_m, \psi_m)$ is used to describe the transformation from the MCMF coordinate system to the inertial selenocentric coordinate system $\mathbf{M}_{\mathrm{MCI}}^{\mathrm{MCMF}}$. The JPL DE provides the Moon libration positions required for the determination of Moon orientation. The DE ephemerides include optical and physical librations. In the transformation from the inertial selenocentric coordinate system to the inertial geocentric coordinate system, $\mathbf{T}_{\mathrm{ECI}}^{\mathrm{MCI}}$, the Moon's position is also derived from the DE. The parameter t represents the coordinated universal time (UTC) time. For the transformation from ECI to ECEF ($\mathbf{M}_{\mathrm{ECEF}}^{\mathrm{ECI}}$), the Earth orientation parameters $(\Pi, \Theta, \mathrm{N}, \mathbf{P})$ are accounted for.

D. Framework of the System

When the time system and reference system transformations are performed, the simulation system is established based on the ephemerides data and these transformations. Fig. 2 shows the framework of the simulation system. There are currently two popular rendering engines for graphics display: OpenGL[1] and DirectX (Microsoft). Because the Microsoft. NET Framework was adopted in this study, the DirectX rendering engines were used to display the Sun–Earth–Moon system. To implement the system, Microsoft C# programming language was chosen and the system was developed under Microsoft. NET Framework. Owing to the evolution and high scalability of C#, some new methods can be used to boost the analysis. Fig. 3 shows the system interface of the simulation system.

[1]Online. [Available]: https://www.opengl.org/

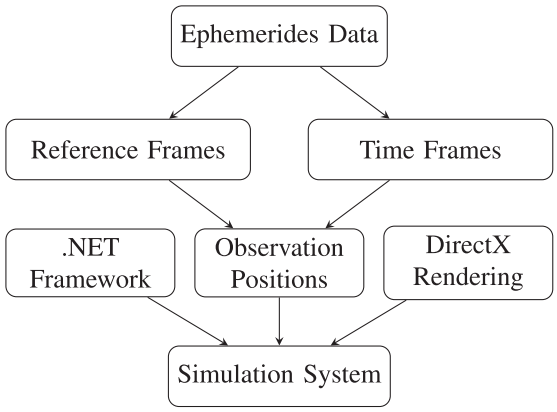

Fig. 2. Flowchart of the simulation system.

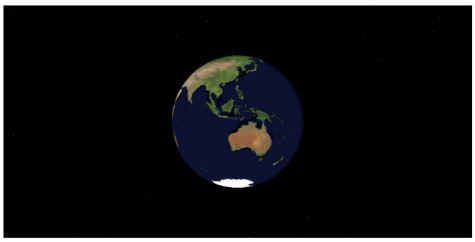

Fig. 3. Interface for the geometry numerical simulation system. The time for the simulation is October 31, 2016, 04:00:00 (UTC), with the MBS located at (0.0°E, 0.0°N).

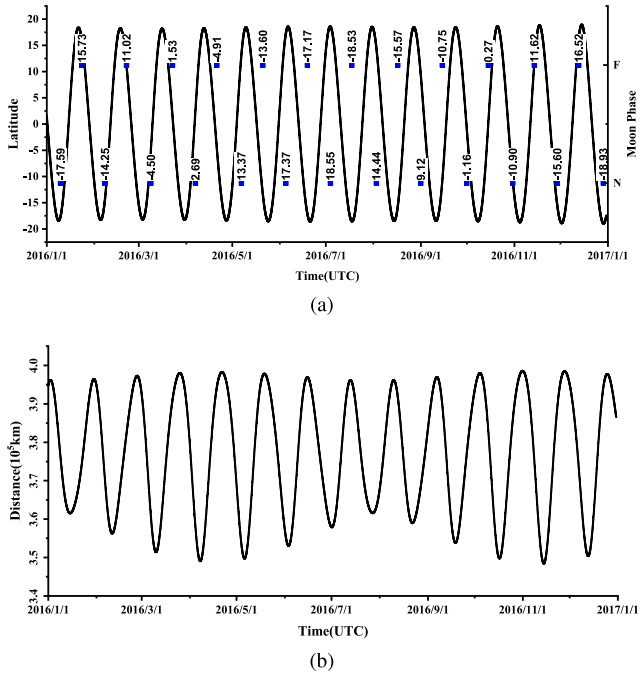

Fig. 4. Subpoints for an MBS at position (0.0°E, 0.0°N) in year 2016: (a) for the latitude and (b) for the orbit altitude. The Moon phases for the new Moon (N) and full Moon (F) are also indicated in (a), and the labels are the corresponding longitudes when the Moon phase occurs.

The simulation system implements the following functions: the time system transformation, the position and velocity extractions for the central bodies, the subpoint analysis, the solar angle analysis, the twilight line analysis, the observation period analysis, and the dynamic display for the analysis results.

III. Simulation and Examples

After establishing the simulation system, we implemented a simulation and analysis using this system and the JPL DE405 data, without using the fixed framework in DE405 or Earth orientation parameter (EOP) data.

A. Subpoint Variation for MBS

Fig. 1 shows the definition of subpoints in this study. The subpoint (X_t, Y_t, H_t) is defined as the projection point of the MBS on the Earth's surface, i.e., the intersection point between the MBS–geocenter line and the Earth's surface. The track of subpoints directly reflects a satellite's transit situation, which is of great significance for the selection of a global control station and for satellite observation.

Using the simulation system, we first analyzed the subpoint variation for MBS. It is well known that owing to the revolution of the Moon and the rotation of the Earth, the longitudes of subpoints are distributed from 180°E to 180°W, so here we will not discuss the variation of subpoint longitudes.

1) Subpoint Variation for MBS in Year 2016: Owing to the regularity of movement of subpoints, here, we take the variation of subpoints in 2016 as an example for detailed analysis. Supposing that a sensor is located at (0.0°E, 0.0°N) on the Moon, we calculated the hourly latitudes and longitudes of the sensor's subpoints. Fig. 4(a) depicts the latitudes of subpoints in 2016 for an MBS located at (0.0°E, 0.0°N), and Fig. 4(b) shows the distance between the MBS and its subpoint.

TABLE I
Monthly Latitude Statistics of Subpoint Locations for an MBS Located at (0.0°E, 0.0°N) in Year 2016

Month	Jan.	Feb.	Mar.	Apr.	May	June
Max—North	18.348	18.226	18.176	18.258	18.419	18.548
Min—South	−18.394	−18.277	−18.213	−18.357	−18.513	−18.59
Mean	−0.719	−0.859	−2.278	−1.809	−1.137	0.204
Month	**July**	**Aug.**	**Sep.**	**Oct.**	**Nov.**	**Dec.**
Max—North	18.571	18.427	18.446	18.588	18.783	18.910
Min—South	−18.545	−18.456	−18.425	−18.522	−18.714	−18.937
Mean	1.594	1.361	−0.043	−1.504	−2.291	−2.868

From Fig. 4(a), we can see that the latitude varied between 18.910°N and 18.937°S and the period is about 27.32 days that shows a type of sinusoidal variation. The northernmost subpoint occurred on December 14, 2016 and the southernmost subpoint on December 29, 2016. However, there was a little difference in the extrema of the latitudes between months (see Table I). From Fig. 4(a) and Table I, we can see that the locations of the subpoints basically exhibit a north–south symmetry.

From Fig. 4(a), we can see that in the year 2016, the corresponding latitudes at which the new and full Moon phase occurs vary regularly. For the new Moon, when the optical remote sensing sensors can observe the whole Earth, the subpoints

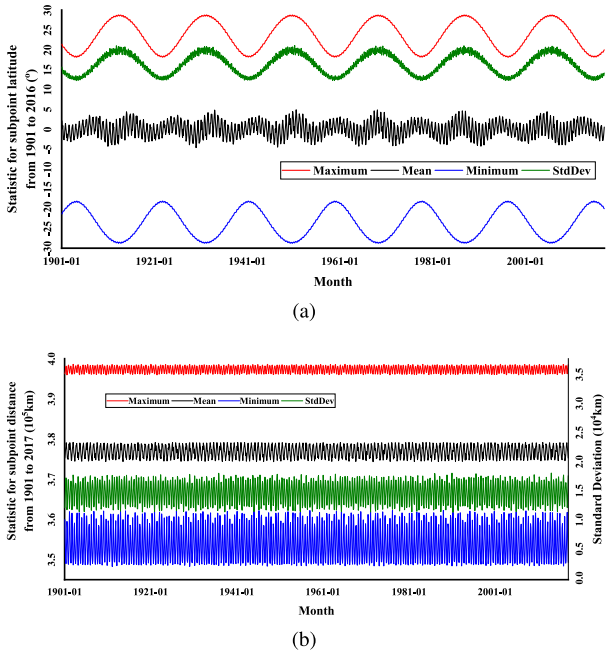

Fig. 5. Monthly mean subpoint latitude for MBS at position (0.0°E, 0.0°N) from 1901 to 2016, the value of Minimum is for the southern latitude and that of Maximum for the northern latitude.

move from the southern to the northern hemisphere, then back to the southern hemisphere. Meanwhile, the subpoints for the full Moon, when the sensors observe the Earth at night, the subpoint movement shows the opposite trend. From April to September 2016, the corresponding subpoints for the new Moon were located in the northern hemisphere, and the smaller local incidence angle was helpful for observing that hemisphere under the Sun. In contrast, from January to March and from September to December, the subpoints were located in the southern hemisphere, which was helpful for observing that hemisphere.

From Fig. 4(b), we can also see that the distance varied between 3.48×10^5 km and 3.98×10^5 km. The shortest distance occurred on November 14, 2016, with subpoint (169.325°W, 13.333°N), when the Moon was the closest to a full supermoon since January 26, 1948, and will not be surpassed until November 25, 2034 [29]. The second shortest distance (3.49×10^5 km) occurred on April 7, 2016, but the Moon was a New Moon. The farthest distance occurred on October 31, 2016, with a subpoint location (110.933°W, 13.328°S).

2) Subpoint Variation for MBS From Year 1901 to 2016: The hourly subpoint latitudes and distance from January 1901 to December 2016 were then simulated and the monthly statistics (mean, standard deviation, maximum, and minimum) for latitude and distance were analyzed (see Fig. 5).

From January 1901 to December 2016, the subpoints for an MBS located at (0.0°E, 0.0°N) moved between 28.770°N and 28.773°S. The northernmost subpoint occurred on March 16, 1913, with its location at (172.130°E, 28.770°N), and 12 days later, the southernmost subpoint occurred on March 28, 1913, with its location at (114.844°E, 28.773°S). The monthly mean latitudes of subpoints varied between 4.856°N and 4.682°S. The

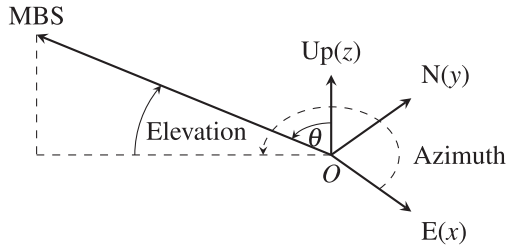

Fig. 6. Diagram for the AEA of a point on the Earth.

maximum, minimum, mean, and standard deviation of the subpoint latitudes show a distinct periodicity. From 1901 to 2016, there are more than six periods of about 18.6 years [5], the period of the Moon's maximum declination angle. The maximum and standard deviation show a similar periodicity, but the minimum shows an opposite periodicity, with a delay of about 14 days. The maximum, minimum, mean, and standard deviation of the subpoint distance do not show any distinct periodicity. The monthly minimum of the subpoint distance has a larger range of variation than the maximum: 13 964.2627 and 2 668.9494 km, respectively.

B. Local Azimuth and Elevation Angle (AEA) for MBS

Fig. 6 shows the set of axes defined by the local East, North, and Up directions at a point with respect to the shape of a central body (Earth) as the point moves over time. The axes is defined as follows: the x-axis points in the local East direction, the y-axis points in the local North direction, and the z-axis points in the direction of the ellipsoidal surface normal that passes through the point. The azimuth is the angular coordinate lying in the xy plane (horizontal plane) measured from the positive x-axis (E) and toward the positive y-axis (N). The elevation is the angular coordinate measured from the xy plane (horizontal plane) and toward the z-axis (Up), which is the angle complementary to the local incidence angle (θ in Fig. 6).

Using the simulation system, after choosing a point of interest on Earth located at (116.276°E, 40.070°N), we simulated the variation for the AEA on July 4, 11, and 18 and November 14, 21, and 29 in the year 2016 (see Fig. 7) with the MBS located at (0.0°E, 0.0°N). The corresponding Moon phases are new Moon, first quarter, full Moon, full Moon, last quarter, and new Moon, respectively (see Fig. 7).

When the Moon phase was a new Moon [see Fig. 7(a) and (f)], the Sun illuminated and the MBS observed the point of interest on Earth almost simultaneously, with similar AEA, and the MBS observed the bright side of the Earth. The elevation angles for the Sun and the MBS were about the same, and the maxima for the Sun and the MBS were larger in summer than in winter. The durations for sunshine and MBS observation were about the same, but longer in summer (about 14 h, 5AM–7PM) than in winter (about 8 h, 8AM–4PM).

When the Moon phase was a full Moon [see Fig. 7(c) and (d)], the Moon rose after sunset. The MBS observed the dark side of the Earth. In summer, the elevation angle for Sun was larger

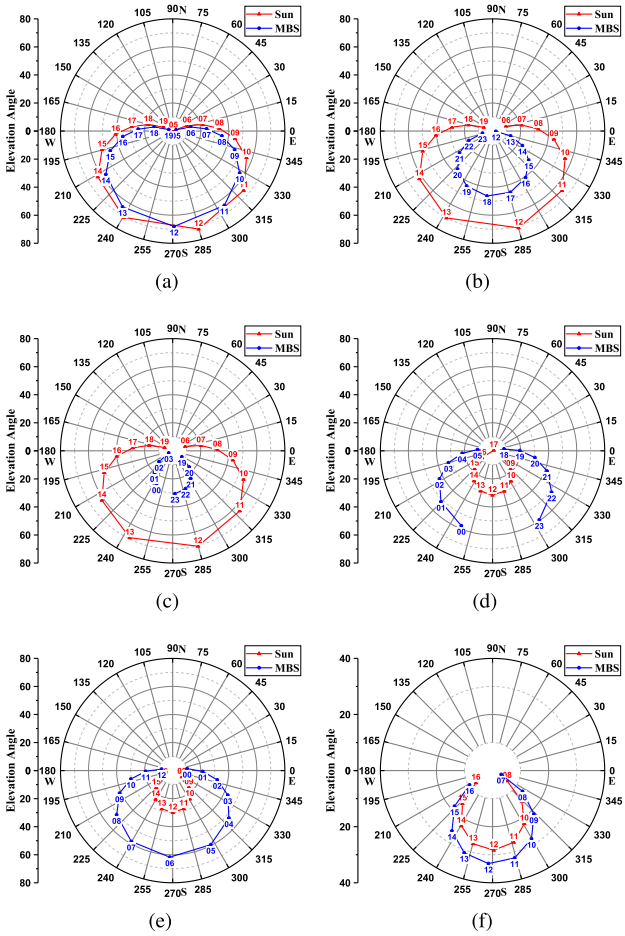

Fig. 7. AEA for a point of interest on the Earth located at (116.276°E, 40.070°N), with the MBS located at (0.0°E, 0.0°N). The numerical labels (05, 06,..., 18, 19) are the local times (hour). The red line is the AEA for the Sun and the blue line for the MBS. Note that because the analysis was performed on just one day's data, the lines between 23PM and 0AM in (c) and (d) are interrupted. (a) July 4, 2016, new Moon. (b) July 11, 2016, first quarter. (c) July 18, 2016, full Moon. (d) Nov. 14, 2016, full Moon. (e) Nov. 21, 2016, last quarter. (f) Nov. 29, 2016, new Moon.

than for MBS, but smaller in winter. In summer, the duration for sunshine (about 13 h, 6AM–7PM) was longer than for the MBS (about 8 h, 7PM–3AM), but was shorter in winter.

When the Moon phase was first or last quarter [see Fig. 7(b) and (e)], the Sun and the MBS appeared 6 hours apart, with the similar AEA to the point of interest on Earth. There was a longer duration of observation in summer (from 5AM to 7PM) than in winter (from 8AM to 4PM). The elevation angle for both of the Sun and the MBS in summer was larger than that in winter.

To master the influence of the motion of the Moon on the changes in the AEA, we simulate the AEA for points of interest on Earth located at sites a (116.276°E, 40.070°N) and b (0.0°E, 0.0°N), with the MBS located at (0.0°E, 0.0°N) in the year 2016 (see Fig. 8). For the point of interest a [see Fig. 8(a)], owing to the northernmost subpoint being at 18.91°N, the azimuth angle for the MBS is mainly distributed between 180° and 360°. The AEA is distributed symmetrically in an east–west direction. The range of elevation angles varies with the azimuth angle, and

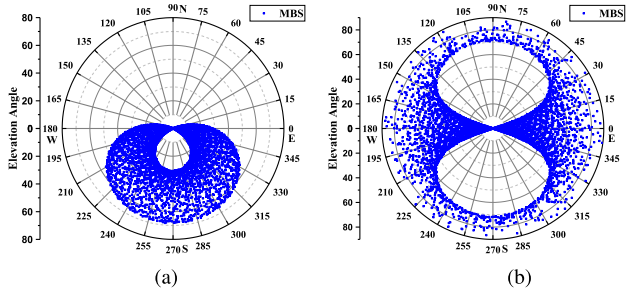

Fig. 8. AEA for points of interest on Earth at (116.276°E, 40.070°N) and (0.0°E, 0.0°N), with the MBS located at (0.0°E, 0.0°N), in the year 2016. (a) (116.276°E, 40.070°N). (b) (0.0°E, 0.0°N).

the elevation angle together with the range reaches a maximum when the azimuth angle is at 270°. For the point of interest b [see Fig. 8(b)], the azimuth angle for the MBS is distributed between 0° and 360°, mainly around the east and west. The AEA is distributed symmetrically in the east–west and south–north directions. The range of elevation angles also varies with the azimuth angle in a different way than the point of interest a. The gap in Fig. 8(a) and the two gaps in Fig. 8(b) reveal that the MBS located at (0.0°E, 0.0°N) cannot observe points of interest on Earth at the special AEA within the gaps in year 2016.

C. Observation Period for Different Points of Interest on Earth

Observation period and duration are two important indicators to measure the performance of the MEO. Here, "observation duration" refers to the visibility time between the MBS sensor and point of interest on Earth when the sighting condition is satisfied.

Although Ren *et al.* and Ye *et al.* have performed similar coverage analyses, their work focused mainly on analysis of spatial coverage, and they treated the Earth as spherical [5], [21]. Here, the reference ellipsoid for Earth is the WGS84 ellipsoid, and the MBS was located at (0.0°E, 0.0°N) rather than at the Moon's center of mass to allow analysis of the observation period for different points of interest on Earth. Taking advantage of the simulation system, the observation periods were analyzed for four different points of interest on Earth [the Equator origin at (0.0°E, 0.0°N), the North Pole at (0.0°E, 90.0°N), the South Pole at (0.0°E, -90.0°N), and the Qinghai Lake at (100.07°E, 36.95°N)] in the year 2016. Here, in order to avoid obstacles caused by natural barriers at too low an elevation, the minimum elevation angle (see Fig. 6) for the MBS is set to 5.0°, which means that points of interest on Earth can only be observed when the MBS is 5.0° higher above the horizontal plane.

1) Observation Period in the Year 2016: Table II shows the number of observations and the total duration for those four points of interest. We can see that as the point of interest on Earth varies from the Equator to the North/South Pole, the observation frequency changes from daily to monthly and the total observation time decreases from 170.736 days to 133.948 days.

TABLE II
OBSERVATION PERIODS AND TOTAL OBSERVATION TIME IN 2016 FOR FOUR DIFFERENT LOCATIONS

Location	Period	Total duration
North Pole (0.0°E, 90.0°N)	Monthly (13 CPs)	133.948 days
Qinghai Lake (100.07°E, 36.95°N)	Almost daily (353 CPs and 1 ICP)	165.674 days
Equator origin (0.0°E, 0.0°N)	Almost daily (353 CPs and 1 ICP)	170.736 days
South Pole (0.0°E, 90.0°S)	Monthly (13 CP and 1 ICP†)	154.628 days

† Complete period (CP) means that both the starting time and end time are in 2016. Incomplete period (ICP) means that the starting time or the end time is not in 2016.

Fig. 9 shows the starting time and the duration for each observation. For the Equator origin, owing to the Earth's rotation and the location of the Equator origin within the subpoint coverage, an MBS can observe the Equator origin almost daily, and therefore, there are 354 observations in the year 2016 with daily observation frequency and a total observation duration of 170.736 days. The longest and shortest durations are 11.639 h (November 14, 2016) and 11.538 h (November 28, 2016), respectively. From Fig. 9(a), the observation duration varies periodically, with 13 cycles. The shortest durations in each cycle are similar (about 11.540 h), but are different (11.605–11.639 h) for the longest duration. The interval between two adjacent longest durations is about 27.32 days.

For the North and South Poles, there are 13 and 14 observations in the year 2016 [see Fig. 9(b)]. The average observation durations are 247.288 h and 265.076 h for the North and South Poles, respectively. The longest and shortest durations for the North Pole occur in February and December 2016 and are 255.398 and 238.525 h, respectively. The longest and shortest durations for the South Pole occur in November and February 2016 and are 280.004 and 259.871 h, respectively. The interval between the starting times of two adjacent observations is around 27.32 days. These observation durations are similar to the polar day/night, but with higher frequencies.

As for the Equator origin, there are 354 observations for Qinghai Lake in the year 2016. From Fig. 9(c), we can see that the observation duration varies periodically, with 13 cycles. The longest and shortest durations are 13.458 h (December 14, 2016) and 9.211 h (December 29, 2016). The interval between two adjacent longest durations is also about 27.32 days. Unlike the Equator origin, the longest and shortest durations in each cycle are similar for Qinghai Lake.

Owing to the sinusoidal nature of the variation of the observation duration for these four locations, the following nonlinear fitting was used to analyze the period for the observation start time–duration curve:

$$y = y_0 + A\sin\left[\frac{\pi(x - x_c)}{w}\right] \tag{5}$$

where $2w$ is the period of the observation duration. The fitting parameters (results) for Fig. 9 are listed in Table III. From

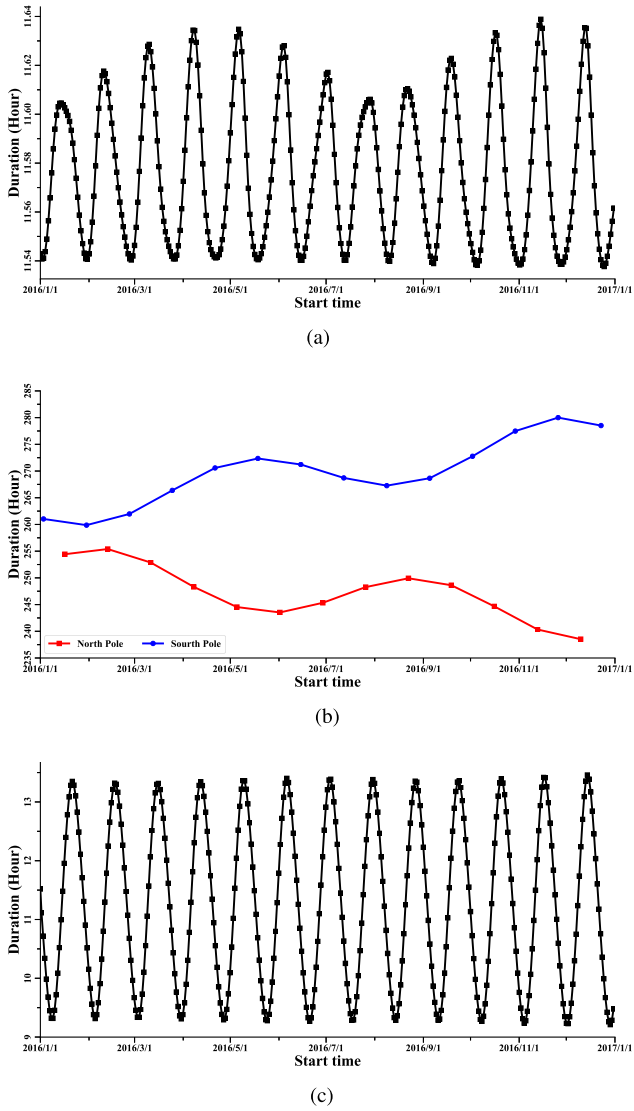

Fig. 9. Observation starting time and duration for each observation for an MBS located at (0.0°E, 0.0°N) in the year 2016. (a) Equator origin. (b) North Pole and South Pole. (c) Qinghai Lake.

Table III, we can see that a high fitting accuracy is obtained, with determination coefficients R^2 greater than 0.6. We can also see that the observation periods for the Equator origin and Qinghai Lake are 27.6 and 27.4 days, respectively, which are close to the 27.32-day period mentioned previously. The observation periods for the North and South Poles are around 191.6 and 197.0 days, respectively.

2) Observation Period From 1901 to 2016: The monthly statistics for observation duration with an MBS located at (0.0°E, 0.0°N) from 1901 to 2016 are shown in Fig. 10.

For the Equator origin [see Fig. 10(a)], the monthly maximum, mean, and minimum values for observation duration vary regularly with about six periods from January 1901 to December 2016. The fluctuations in the maximum value are more volatile. The standard deviation (StdDev) of the observation duration remains nearly constant, with a slight fluctuation around 0.03. The longest and shortest durations are 11.64 h (starting on

TABLE III
NONLINEAR FITTING PARAMETERS FOR OBSERVATION PERIODS IN 2016 FOR FOUR DIFFERENT LOCATIONS

Figure	Location	Parameters					Period
		y_0	x_c	w	A	R^2	$2w$
9a	Equator origin	11.577	51969.569	13.793	0.041	0.927	27.6
9b	North Pole	247.156	−189078.152	95.831	5.912	0.765	191.6
	South Pole	269.772	−73660.681	98.480	6.650	0.622	197.0
9c	Qinghai Lake	11.294	71490.409	13.672	2.009	0.995	27.4

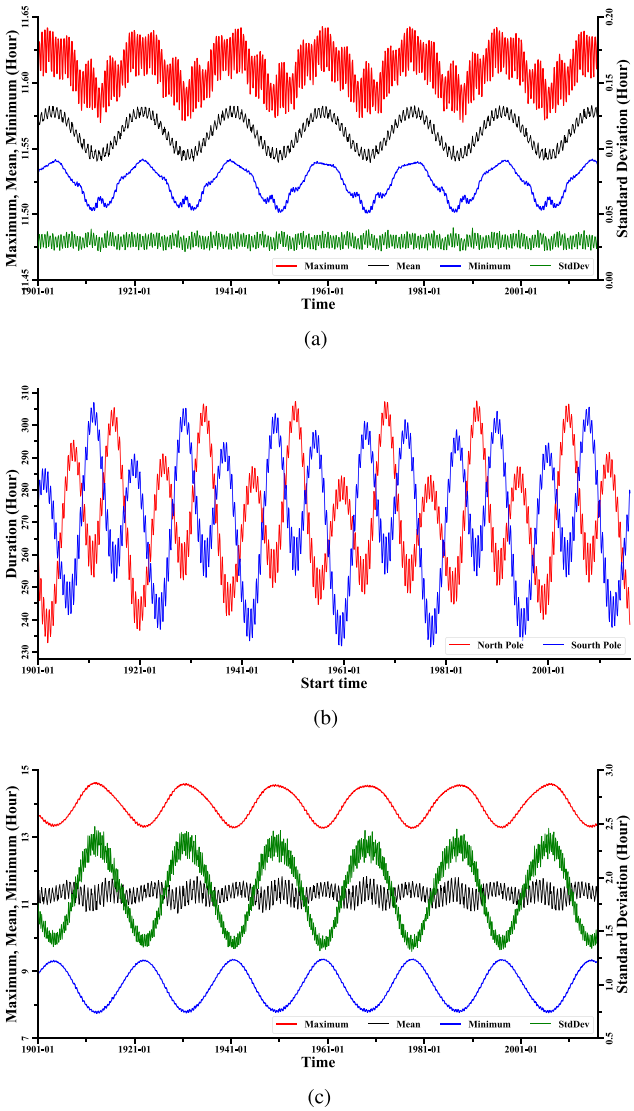

Fig. 10. Monthly statistics for observation duration with MBS located at (0.0°E, 0.0°N) from 1901 to 2016. Because of the monthly observations for the North and South Poles, the statistics are not provided. (a) Equator origin. (b) North and South Poles. (c) Qinghai Lake.

November 30, 1959 06:10:21) and 11.50 h (starting at July 13, 1969 05:28:30), respectively.

Because of the monthly observation for the North and South Poles, the actual observation durations rather than the statistics are provided [Fig. 10(b)]. There are 13 periods for the observation duration for both the North and South Poles from January 1901 to December 2016 [Fig. 10(b)], but with the opposite trends. The longest and shortest durations for the North Pole start on December 10, 1986, 15:36:00 and on December 10, 1902, 09:15:16, and are 307.47 and 232.86 h, respectively. The longest and shortest durations for the South Pole start on December 14 21:27:20 and December 6, 1977 11:09:38, and are 307.00 and 231.56 h, respectively.

There are also six cycles for the maximum, minimum, and StdDev of the observation duration for Qinghai Lake from January 1901 to December 2016 [see Fig. 10(c)], with smooth fluctuations. There are up to 13 cycles for the mean values. The longest and shortest durations are 14.63 h (January 20, 1913, 8:12:03) and 7.74 h (March 28, 1913, 19:9:4), respectively. Compared with the Equator origin, the lines for the Qinghai Lake are smoother.

Here, we also use the nonlinear fitting in (5) to analysis the observation period. The fitting parameters (results) for Fig. 10 are listed in Table IV, where we can see that high fitting accuracy is obtained, with all the determination coefficients R^2 greater than 0.5. Owing to the volatile fluctuations of the monthly maximum observation duration for the Equator origin, the R^2 is a little lower than for the others. Meanwhile the monthly StdDev has no obvious period, and the R^2 is also lower. The monthly mean of the observation duration for the Qinghai Lake is stable and so has a lower R^2 and no obvious period.

We can also see that the observation periods for the Equator origin and Qinghai Lake are about 18.6 years, close to the 18.6-year period mentioned previously. Unlike these two locations, the observation periods for the North and South Poles are about 8.8 years.

IV. ANALYSIS AND DISCUSSION

A. Comparison Between Different DE Data Sources

There are many kinds of planetary ephemeris. The accuracy of the geometric simulation and analysis for the MEO is directly determined by the planetary ephemeris data. Therefore, before any geometric analysis of Earth observation, the order of influence of different ephemerides on the geometric error of observation should be clarified.

As mentioned previously, the simulations in Section III were done using JPL DE405 data. In our simulation system, three kinds of DE data can be used, including STK numerical analysis data, JPL DE405 data, and DE421 data. Here, the influences

TABLE IV
NONLINEAR FITTING PARAMETERS FOR OBSERVATION PERIODS FROM JANUARY 1901 TO DECEMBER 2016 FOR FOUR DIFFERENT LOCATIONS

Figure	Location	Statistics	Parameters					Period
			y_0	x_c	w	A	R^2	$2w/365$
10a	Equator origin	Maximum	11.610	89174.728	3400.047	0.017	0.500	18.630
		Mean	11.561	96884.511	3398.723	0.017	0.946	18.623
		Minimum	11.523	90327.141	3398.377	0.017	0.957	18.621
		StdDev	0.030	-2555.501	102.946	0.005	0.860	0.564
10b	North Pole		271.867	33633.177	1608.179	21.286	0.748	8.812
	South Pole		271.472	11950.738	1621.598	23.043	0.732	8.885
10c	Qinghai Lake	Maximum	13.974	94435.068	3397.367	0.628	9.989	18.616
		Mean	11.312	-3595.964	133.438	0.253	0.662	0.731
		Minimum	8.548	90773.383	3397.748	0.764	0.997	18.618
		StdDev	1.878	94297.611	3397.565	0.456	0.958	18.617

TABLE V
COMPARISON OF MBS'S POSITION AND THE AED OF A POINT OF INTEREST ON EARTH SIMULATED USING DIFFERENT DE AND EOP DATA ON DECEMBER 3, 2017, 16:07:24

Type	Combination			Position			AED		
	JPL DE	FF[‡]	EOP	Longitude	Latitude	Altitude (km)	Azimuth	Elevation	Distance (km)
1	DE405	Yes	Yes	116.493190	17.628669	349 859.6271	179.457734	67.161406	350 349.2426
2	DE405	Yes	No	116.494212	17.628596	349 859.6271	179.455183	67.161324	350 349.2461
3	DE405	No	Yes	116.493257	17.628784	349 859.5460	179.457565	67.161522	350 349.1566
4	DE405	No	No	116.494279	17.628711	349 859.5460	179.455014	67.161441	350 349.1600
5	DE421	Yes	Yes	116.493184	17.628670	349 859.6281	179.457748	67.161407	350 349.2436
6	DE421	Yes	No	116.494207	17.628597	349 859.6281	179.455197	67.161325	350 349.2470
7	DE421	No	Yes	116.493258	17.628785	349 859.5465	179.457560	67.161523	350 349.1570
8	DE421	No	No	116.494281	17.628712	349 859.5464	179.455009	67.161441	350 349.1605
9	STK	N/A	Yes	116.460690	17.632845	349 982.2032	179.538805	67.166012	350 471.6268
10	STK	N/A	No	116.461712	17.632772	349 982.2032	179.536254	67.165931	350 471.6302

[‡]FF: JPL DE fixed framework for the Moon.

of the different data sources on the geometric simulation and analysis will be discussed. Meanwhile, the influence of the EOP and the JPL DE fixed framework will also be discussed, since the JPL DE framework for the Moon is related to the libration and nutation of the Moon. Here, we focus on the MBS's position (0.0°E, 0.0°N) in the Earth-fixed framework and the azimuth–elevation–distance (AED) for a point of interest on Earth located at (116.276°E, 40.070°N). The simulation results for December 3, 2017, 16:07:24 are listed in Table V and Fig. 11.

Table V and Fig. 11 confirm that for JPL DE data, the MBS's position and the AED for the point of interest on Earth vary slightly, regardless of whether a fixed framework or EOP data are used, and the same applies for STK data. However, the MBS's position and the AED for the point of interest on the Earth simulated using the JPL DE data are obviously different from those simulated using the STK numerical analysis data.

B. Influence of Minimum Observation Elevation Angle

As mentioned previously, the observation period simulations in Section III-C were done with a minimum elevation angle for the MBS of 5.0° in order to avoid obstacles caused by natural barriers at too low an elevation. The minimum elevation angle for the MBS influences the observation duration, and thus,

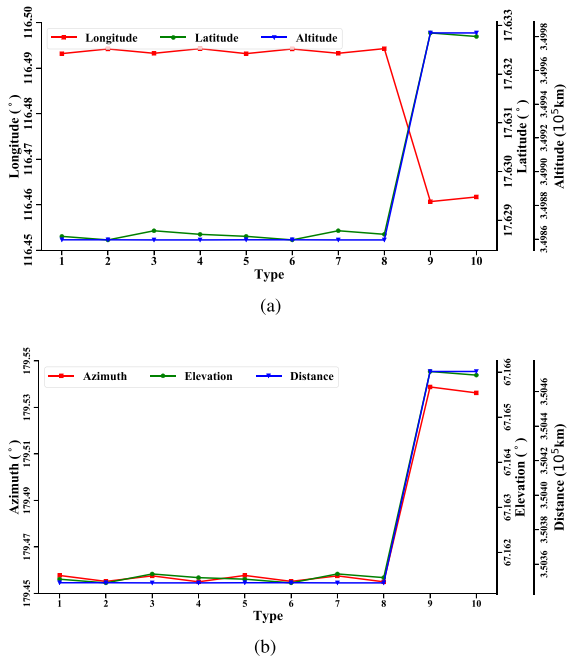

Fig. 11. Difference of MSB's position and AED for a point of interest on Earth under different DE and EOP data. (a) Position. (b) AED.

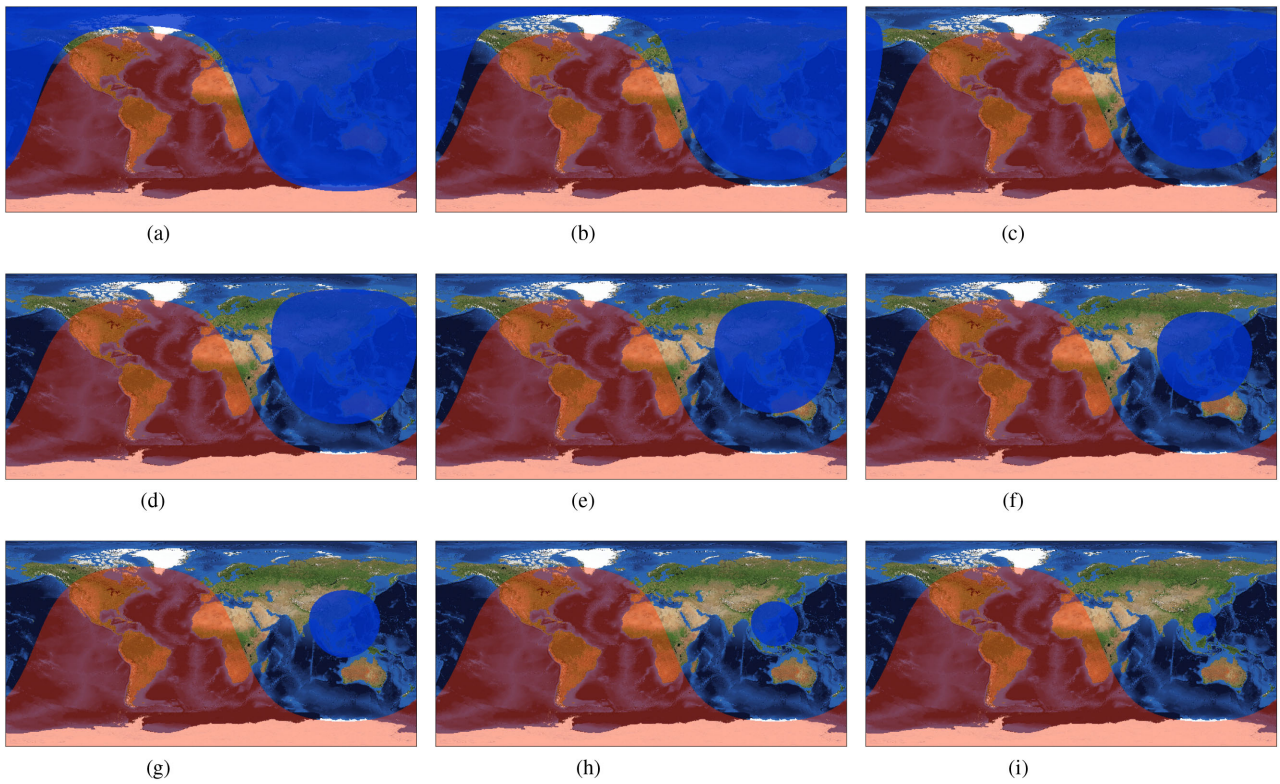

Fig. 12. Observation extent for different minimum observation elevation angles for an MBS located at (0.0°E, 0.0°N) at Dec. 3, 2017, 16:07:24. (a) 0°, 49.32%. (b) 10°, 40.60%. (c) 20°, 32.23%. (d) 30°, 24.38%. (e) 40°, 17.41%. (f) 50°, 11.37%. (g) 60°, 6.50%. (h) 70°, 2.91%. (i) 80°, 0.73%.

the observation extent directly, so here, we will focus on the influence of the minimum observation elevation angle.

The MBS observation extent is defined as the region of the Earth where the MBS is seen at a minimum predefined elevation angle. Usually, the MBS observation extent or the MBS footprint can be expressed as a fraction (percentage) of the Earth's area.

$$\text{Coverage}(\%) = \frac{S_{\text{Coverage}}}{S_{\text{Earth}}} = \frac{\text{total coverage pixels}}{\text{total image pixels}} \quad (6)$$

where the total coverage pixels and the total image pixels are both relative to the image resolution and the image projection.

Here, the simulated observation extent images with a pixel resolution of 0.5° are stored in the WGS84 Geographic Coordinate System and shown in the Plate Carree Projection System. Fig. 12 shows the observation extent for different minimum observation elevation angles for an MBS located at (0.0 °E, 0.0 °N) on December 3, 2017, 16:07:24. The red region represents the sunlight extent, and the blue region for the MBS observation extent. These images confirm that as the minimum elevation angle increases, the observation extent decreases, with the coverage dropping from 49.32% to 0.49%.

The satellite's observation extent is determined by its observation distance and also the minimum elevation angle [30]. With the revolution and rotation of the Moon itself, the position and observation distance of an MBS are also changing [see Fig. 4(b)]. Fig. 13(a) shows the variation of the MBS orbital altitude and the observation extent coverage with a minimum elevation angle of

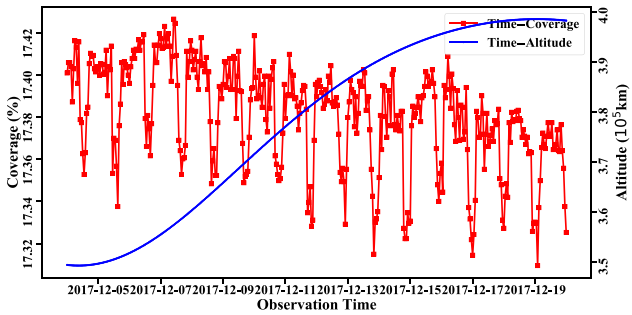

(a)

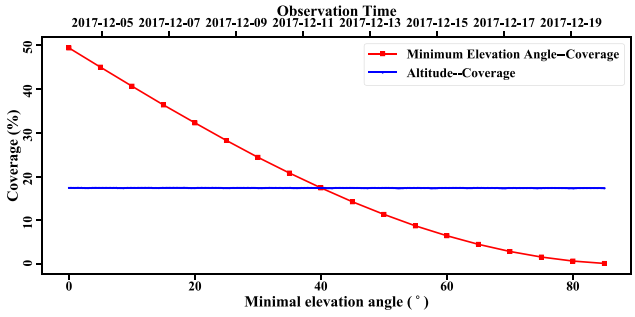

(b)

Fig. 13. Influence of the orbital altitude and minimum elevation angle on the observation extent coverage. (a) Influence of the orbital altitude with minimum elevation angle of 40°. (b) Comparison of the influence of the orbital altitude from (a) and that of minimum elevation angle (see Fig. 12).

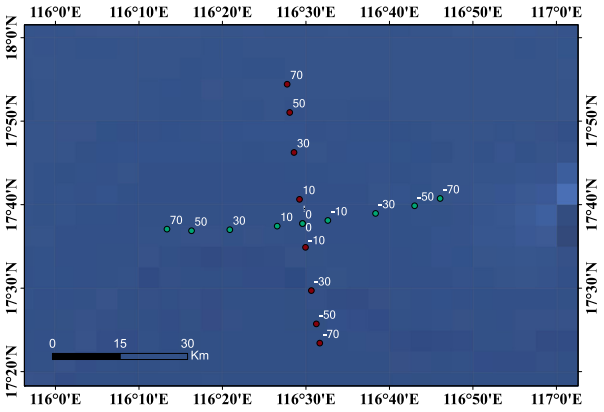

Fig. 14. Subpoints for an MBS at different locations on December 3, 2017, 16:07:24. The numerical labels represent the MBS location, which varies from (0°E, 70°S) to (0°E, 70°N) (the vertical points) and from (70°E, 0°N) to (70°W, 0°N) (the horizontal points).

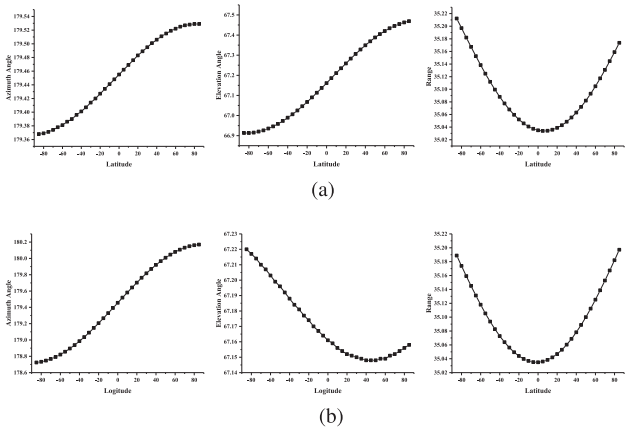

Fig. 15. AED with an MBS at different locations for a point of interest on the Earth at (116.276°E, 40.070°N) on December 3, 2017, 16:07:24. The MBS location varies from (0°E, 70°S) to (0°E, 70°N) (a) and from (70°E, 0°N) to (70°W, 0°N) (b). (a) MBS with longitude 0°. (b) MBS with latitude 0°.

40° from December 4, 2017 to December 19, 2017, a half cycle in Fig. 4(b). Fig. 13(a) confirms that as the orbit altitude rises from 3.49×10^5 to 3.98×10^5 km [close range as in Fig. 4(b)], the coverage is reduced from 17.43% to 17.32%. Comparing the influence of the orbital altitude and minimum elevation angle on the observation extent coverage, we can conclude that the influence of the observation distance on the observation extent is much smaller than that of the minimum elevation angle, mainly because of the relatively long observation distance of about 380 000 km for an MBS.

C. Influence of MBS Location

1) Influence of MBS Location on Subpoint: The definition of the MBS subpoint is shown in Fig. 1. The subpoint (X_t, Y_t, H_t) is defined as the projection point of the MBS on the Earth's surface, i.e., the point of intersection of the MBS–geocenter line and the Earth's surface.

To evaluate the influence of different MBS locations on the MBS subpoint, the MBS is assumed to be deployed on the Moon's near side. As the MBS moves to different locations, the subpoints will vary in a circle on the Earth's surface. Fig. 14 shows the MBS subpoints on December 3, 2017, 16:07:24, as the MBS location varies from (0°E, 70°S) to (0°E, 70°N) and from (70°E, 0°N) to (70°W, 0°N). As the location of the MBS changes, the location of the subpoint of the MBS, and consequently, the AED of the point of interest on Earth, and the observation period and duration also change slightly. From Fig. 14, we can see that the subpoints vary on a circle of radius 30 km. This means that if the resolution of the MEO images is worse than 60 km, the position error will be less than one pixel.

2) Influence of MBS Location on Local Elevation Angle: The definition of the local AED of a point of interest on the Earth is shown in Fig. 6. To evaluate the influence of different MBS locations on the local AED, the MBS is assumed to be deployed on the Moon's near side to ensure the visibility between the MBS and the point of interest.

Fig. 15 shows the local azimuth angle, elevation angle, and distance for a point of interest on the Earth located at (116.276°E, 40.070°N) on December 3, 2017, 16:07:24. As the MBS location varies from (0°E, 70°S) to (0°E, 70°N) and from (70°E, 0°N) to (70°W, 0°N), the trends of the azimuth angle and range are similar, but differ from that of the elevation angle. The range of variation of the azimuth angle is 0.18° as the MBS location varies from (0°E, 70°S) to (0°E, 70°N), which is much smaller for that (1.5°) from (70°E, 0°N) to (70°W, 0°N). The trend of the elevation angle is opposite. As the MBS location varies from (0°E, 70°S) to (0°E, 70°N), the elevation angle increases steadily from 66.92° to 67.45°. The trend of the distance is similar to that of the azimuth angle: it goes down steadily from (0°E, 70°S) and (70°W, 0°N) to near (0°E, 0°N), and then, rises steadily, from which it can be concluded that as the MBS location moves around from (0°E, 0°N), the observation distance increases. The small ranges of variation of the azimuth, elevation angle, and distance are also introduced by the distance between the MBS and the point of interest on the Earth, which is much greater than the distances between the MBS locations.

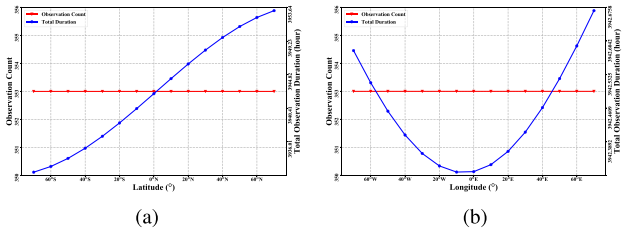

Fig. 16. Total observation duration in the year 2018 with an MBS at different locations for a point of interest on Earth at (116.276°E, 40.070°N). The MBS location varies from (0°E, 70°S) to (0°E, 70°N) (a) and from (70°E, 0°N) to (70°W, 0°N) (b). (a) MBS with longitude of 0°. (b) MBS with latitude of 0°.

3) Influence of MBS Location on Observation Period: Fig. 16 shows the total observation duration for a point of interest on the Earth located at (116.276°E, 40.070°N) in the year 2018, with the MBS at different locations varying from (0°E, 70°S) to (0°E, 70°N) and from (70°E, 0°N) to (70°W, 0°N). It can be seen that wherever the sensors are deployed on the near side of the Moon, the point of interest on the Earth can be observed 353 times (not 365 times) in 2018. The trends for the total observation duration

are distinct. The duration increases steadily as the MBS location moves from (0°E, 70°S) to (0°E, 70°N). However, it decreases as the MBS location moves from (70°W, 0°N) to (0°E, 0°N) and increases as the location moves from (0°E, 0°N) to (70°E, 0°N). We can also see that the change of observation duration caused by a change in latitude of the MBS location is greater than that caused by east–west movement. As the MBS moves from south to north [see Fig. 16(a)], the maximum observation duration (3953.212 h) occurs at (0°E, 70°N) and the minimum duration (3932.024 h) at (0°E, 70°S), with a range of about 21.188 h. As the MBS moves from west to east [see Fig. 16(b)], the maximum observation duration (3942.669 h) occurs at (70°E, 0°N) and the minimum duration (3942.325 hours) at (10°W, 0°N), with a range of about 0.344 h.

V. Conclusion

The study of Earth's macroscopic scientific phenomena and large-scale continuous global change needs more and more large-scale and multilayer Earth observations. Meanwhile, the study on the Earth's radiation budget, Earth's ionosphere, the EUV radiation properties of the Earth's plasmasphere also needs to observe the Earth as a whole from a longer distance.

The Moon is the only natural satellite of the Earth, and it is feasible to deploy sensors on its surface for Earth observations. Compared to the spaceborne satellite, the MEO can observe the Earth as a whole, and will also provide much wider coverage and higher temporal resolution. The multisensor joint observation from the MEO can provide information for studying the multilayer interaction of the Earth. With the successful implementation of the Moon exploration and Moon landing programs, the MEO will also be realized in the next few decades. By then, various sensors will be deployed on the Moon's surface to provide more unique data for Earth Observations.

Whatever sensors are arranged on the Moon, the Sun–target (Earth)–sensor (MBS) geometry is a precondition for understanding the MEO. The geometry simulation and analysis for the MEO will provide more support for the design of the MBS system parameters and the site selection for the MBS. Here, we have proposed a geometry numerical simulation system for the MEO, combining JPL DE data and the Microsoft. NET Framework.

Some simulations have been performed using this simulation system, including those of subpoint variations, the local AEA, and the observation period. The results show that when an MBS is deployed, its subpoint moves between 28.770°N and 28.773°S. However, wherever the MBS is deployed, there is an immutable period of 27.32 days for Earth observation, which is determined by the period of the Moon's revolution around the Earth. An MEO can realize continuous observations at multiple angles for the same point of interest on the Earth over a long time. It can revisit low latitude regions every day and the polar regions every month, with each observation time being up to 250 h.

Some factors influencing the MEO geometry have also been analyzed. For regular research, STK numerical analysis data, JPL DE405 data, and DE421 data are sufficiently accurate. However, for more precise geometric positioning, more advanced ephemeris data are needed. Taking account of nutation, libration, and EOP data can improve the accuracy of mathematical expressions for the MEO geometry. From a comparison of the influence of the orbital altitude and minimum elevation angle on the observation extent coverage, we can conclude that the observation distance has much less influence than the minimum elevation angle, mainly because of the relatively long observation distance of about 380 000 km for an MBS. Wherever an MBS is deployed on the near-side of the Moon, its subpoints lie in a circle of radius of 30 km on the Earth's surface, which means that if the resolution of an MEO image is worse than 60 km, the position error will be less than one pixel. When an MBS is located on the near-side of the Moon, the ranges of variation of the azimuth angle, elevation, and range for a point of interest on Earth are small because the distance between the MBS and a point of interest on the Earth is much greater than the distances between MBS locations. Changes in observation duration caused by south–north movement of the MBS are greater than those caused by east–west movements.

In conclusion, as a consequence of the geometrical relationships between the Sun, Earth, and Moon, the Moon represents a special platform that can be used to observe large-scale geoscientific phenomena with long-term consistency, integrity, stability, and uniqueness.

Acknowledgment

The authors would like to thank JPL for providing the DE data and the anonymous reviewers for helpful suggestions.

References

[1] H. Guo, Y. Ding, G. Liu, D. Zhang, W. Fu, and L. Zhang, "Conceptual study of lunar-based SAR for global change monitoring," *Sci. China Earth Sci.*, vol. 57, no. 8, pp. 1771–1779, 2014.

[2] H. Guo, G. Liu, Y. Ding, Y. Zou, and S. Huang, "Moon-based earth observation for large scale geoscience phenomena," in *Proc. IEEE Int. Geosci. Remote Sens. Symp.*, Beijing, China, 2016, pp. 3705–3707.

[3] W. B. Parks, V. Meadows, P. Mccullough, M. Postman, B. Bussey, and C. Christian, "Lunar based observations of the earth as a planet," in *Proc. Astrobiol. Sci. Conf.*, 2010, Art. no. 98195.

[4] Y. Ren, H. Guo, G. Liu, H. Ye, and Y. Ding, "Simulation of moon-based observation for large-scale earth science phenomena," in *Proc. IEEE Int. Geosci. Remote Sens. Symp.*, Beijing, China, 2016, pp. 6253–6256.

[5] Y. Ren, H. Guo, G. Liu, and H. Ye, "Simulation study of geometric characteristics and coverage for moon-based earth observation in the electro-optical region," *IEEE J. Sel. Topics Appl. Earth Observ. Remote Sens.*, vol. 10, no. 6, pp. 2431–2440, Jun. 2017.

[6] L. Cao *et al.*, "LUT: A lunar-based ultraviolet telescope," *Sci. China Phys., Mech. Astron.*, vol. 54, no. 3, pp. 558–562, 2011.

[7] F. He, B. Chen, and X. Zhang, "Moon-based imaging of earth plasmaspheric extreme ultraviolet radiation," *Opt. Precis. Eng.*, vol. 18, no. 12, pp. 2564–2573, 2010.

[8] Z. Li, "Opto-mechanical design of lunar based EUV camera for imaging the Earth," *Chin. J. Sci. Instrum.*, vol. 31, no. 10, pp. 2352–2356, 2010.

[9] Z. Li and B. Chen, "Design and analysis of lunar based tracking turntable for Earth observation," *Acta Photonica Sinica*, vol. 39, no. 12, pp. 2215–2219, 2010.

[10] S. Li, Q. Wu, and X. Yang, "Thermal design and thermal analysis for the moon-landed telescope," *Opt. Techn.*, vol. 37, no. 01, pp. 80–84, 2011.

[11] S. Li, Q. Wu, X. Yang, and B. Chen, "Thermal design and computer simulation for Moon-landed explorer," *Comput. Eng. Des.*, vol. 32, no. 06, pp. 2083–2087, 2011.

[12] C. Nie, J. Liao, G. Shen, and W. Duan, "Simulation of the land surface temperature from moon-based earth observations," *Adv. Space Res.*, 2018, doi: 10.1016/j.asr.2018.09.041.
[13] W. Duan, S. Huang, and C. Nie, "Conceptual design of a moon-based earth radiation observatory," *Int. J. Remote Sens.*, vol. 39, no. 18, pp. 5834–5849, 2018.
[14] W. Duan, S. Huang, and C. Nie, "Entrance pupil irradiance estimating model for a moon-based earth radiation observatory instrument," *Remote Sens.*, vol. 11, no. 5, pp. 583-1–583-18, 2019, doi: 10.3390/rs11050583.
[15] G. Fornaro, G. Franceschetti, F. Lombardini, A. Mori, and M. Calamia, "Potentials and limitations of moon-borne SAR imaging," *IEEE Trans. Geosci. Remote Sens.*, vol. 48, no. 7, pp. 3009–3019, Jul. 2010.
[16] Y. Ding, H. Guo, and G. Liu, "Method to estimate the doppler parameters of moon-borne SAR using JPL ephemeris," *J. Beijing Univ. Aeronaut. Astronaut.*, vol. 41, no. 01, pp. 71–76, 2015.
[17] A. Moccia and A. Renga, "Synthetic aperture radar for earth observation from a lunar base: Performance and potential applications," *IEEE Trans. Aerosp. Electron. Syst.*, vol. 46, no. 3, pp. 1034–1051, Jul. 2010.
[18] Z. Xu and K. Chen, "On signal modeling of moon-based synthetic aperture radar (SAR) imaging of earth," *Remote Sens.*, vol. 10, no. 3, pp. 486-1–486-24, 2018, doi: 10.3390/rs10030486.
[19] D. Zhang, "Study on methodology of lunar-based earth observation for global change," Ph.D. dissertation, East China Normal Univ., Shanghai, China, 2012.
[20] J. Walker, "Home planet," 2006. [Online]. Available: http://www.fourmilab.ch/homeplanet/
[21] H. Ye, H. Guo, G. Liu, and Y. Ren, "Observation scope and spatial coverage analysis for earth observation from a moon-based platform," *Int. J. Remote Sens.*, vol. 39, pp. 1–25, 2017, doi: 10.1080/01431161.2017.1395976.
[22] Y. Ding, H. Guo, and G. Liu, "Coverage performance analysis of earth observation from lunar base for global change detection," *J. Hunan Univ.*, vol. 41, no. 10, pp. 96–102, 2014.
[23] H. Ye, H. Guo, and G. Liu, "Observation parameters design of moon-based earth observation sensors for monitoring three-polar regions," in *Proc. IEEE Int. Geosci. Remote Sens. Symp.*, Fort Worth, TX, USA, 2017, pp. 5755–5778.
[24] Wikipedia, "Ephemeris," 2018. [Online]. Available: https://en.wikipedia.org/wiki/Ephemeris
[25] Wikipedia, "Jet propulsion laboratory development ephemeris," 2018. [Online]. Available: https://en.wikipedia.org/wiki/Jet_Propulsion_Laboratory_Development_Eph emeris
[26] W. M. Folkner, J. G. Williams, and D. H. Boggs, "The planetary and lunar ephemeris DE 421," *Interplanetary Netw. Prog. Rep.*, vol. 178, pp. 1–34, 2009.
[27] E. M. Standish, X. X. Newhall, and J. G. Williams, JPL Planetary and Lunar Ephemerides (CD-ROM). Richmond, VA, USA: Willmann-Bell, Inc., 1997.
[28] H. Ye, H. Guo, G. Liu, and Y. Ren, "Observation duration analysis for earth surface features from a moon-based platform," *Adv. Space Res.*, vol. 62, no. 2, pp. 274–287, 2018.
[29] Wikipedia, "Supermoon," 2018. [Online]. Available: https://en.wikipedia.org/wiki/Supermoon
[30] S. Cakaj, B. Kamo, A. Lala, and A. Rakipi, "The coverage analysis for low earth orbiting satellites at low elevation," *Int. J. Adv. Comput. Sci. Appl.*, vol. 5, no. 6, pp. 6–10, 2014.

Guozhuang Shen (Member, IEEE) received the B.S. degree from Zhejiang University, Hangzhou, China, in 2003, and the Ph.D. degree in geographic information system from the Institute of Remote Sensing Applications, Chinese Academy of Sciences, Beijing, China, in 2008.

He currently working with the Key Laboratory of Digital Earth Science, Aerospace Information Research Institute, Chinese Academy of Sciences. His research interests include microwave remote sensing for lake/wetland ecosystems, and Moon-based remote sensing.

Huadong Guo (Member, IEEE) received the bachelor's degree in geology from the Geology Department, Nanjing University, Nanjing, China, in 1977, and the M.Sc. degree in geographic information system from the University of Chinese Academy of Sciences (CAS), Beijing, China, in 1981.

He was a Project Leader for more than ten key programs related to Earth observation. Since the past ten years, he has been one of the principal investigators for SIR-C/X-SAR, JERS-1 SAR, ERS- 1/2 SAR, Radarsat-1/2, Envisat, SRTM, and ALOS programs. He is a Guest Professor with seven universities in China. From 1996 to 2000, he was the Principal Scientist with the Expert Group for Information Acquisition and Processing Technology, National High-tech Research and Development Program in China. He has authored or coauthored more than 200 papers and 17 books.

Mr. Guo was the recipient of three national awards on science and technology and nine awards by the CAS. He is a member of the International SAR Working Group, a member of CoDATA Executive Committee, the Chairman of the Associate on Environment Remote Sensing of China, the Secretary General of the International Society for Digital Earth, and the Editor-in-Chief for the *International Journal of Digital Earth and Big Earth Data*.

Guang Liu (Member, IEEE) received the B.S. and M.S. degrees in physics from Tsinghua University, Beijing, China, in 1999 and 2002, respectively, and the Ph.D. degree in geographic information system from the Institute of Remote Sensing Applications, Chinese Academy of Sciences (CAS), Beijing, China, in 2008.

From 2006 to 2007, he was a Guest Researcher with the Mathematical Geodesy and Positioning, Delft University of Technology, Delft, The Netherlands, where he was involved with the time-series analysis of phased array type L-band Synthetic aperture radar (SAR) data. He is currently a Professor with the Institute of Remote Sensing and Digital Earth, CAS. His research interests include the study of feasibility and potential applications of SAR image time-series analysis, moon-based earth observation conceptual studies, and land surface deformation, glacier change, and landslide studies.

Lu Zhang (Member, IEEE) received the Ph.D. degree in SAR remote sensing from the Institute of Remote Sensing Application, Chinese Academy of Sciences (CAS), Beijing, China, in 2008.

He is an Associate Professor with the Key Laboratory of Digital Earth Science, Aerospace Information Research Institute, CAS. He was a Visiting Scientist with the Institute of Telecommunication and Electric of Rennes, University of Rennes 1, Rennes, France, in 2013. He is the author of 80 journal papers for SAR remote sensing. His research interests include SAR image processing, information extraction and physical parameter estimation model, and moon-based remote sensing.

Jing Huang received the bachelor's degree in geomatics from the China University of Geosciences, Wuhan, China, in 2018. She is currently working toward the Ph.D. degree in geographical information system with the Institute of Remote Sensing and Digital Earth, Chinese Academy of Sciences, Beijing, China.

Her research interests include the study of the Moon-based observation platform, including the observation geometry, the moon-based radiometer's design, and its related applications.